Computational quantification of patient specific changes in ventricular dynamics associated with pulmonary hypertension

Henrik Nicolay Topnes Finsberg, Joakim Sundnes, Ce Xi, Lik Chuan Lee, Xiaodan Zhao, Ju Le Tan, Martin Genet, Liang Zhong, Samuel Thomas Wall

Computational quantification of patient specific changes in ventricular dynamics associated with pulmonary hypertension

Henrik Finsberg* and Joakim Sundnes

Simula Research Laboratory, Oslo, Norway

Center for Cardiological Innovation,

Songsvannsveien 9, 0372 Oslo, Norway and

Department of Informatics, University of Oslo,

P.O. Box 1080, Blindern 0316 Oslo, Norway

Ce Xi* and Lik Chuan Lee

Department of Mechanical Engineering,

Michigan State University, East Lansing, U.S.A

Xiaodan, Zhao and Ju Le Tan

National Heart Center Singapore, Singapore

Martin Genet

Mechanics Department and Solid Mechanics Laboratory (LMS),

École Polytechnique / CNRS / Paris-Saclay University, Palaiseau, France and

M3DISIM research team, INRIA / Paris-Saclay University, Palaiseau, France

Liang Zhong

National Heart Center Singapore, Singapore and

Duke-NUS Medical School,Singapore

Samuel T. Wall

Simula Research Laboratory, Oslo, Norway and

Center for Cardiological Innovation,

Songsvannsveien 9, 0372 Oslo, Norway

ABSTRACT

Pulmonary arterial hypertension (PAH) causes an increase in the mechanical loading imposed on the right ventricle (RV) that results in progressive changes to its mechanics and function. Here, we quantify the mechanical changes associated with PAH by assimiliating clinical data consisting of reconstructed 3D geometry, pressure and volume waveforms as well as regional strains measured in PAH patients ($n = 12$) and controls ($n = 6$) within a computational modeling framework of the ventricles. Modeling parameters reflecting regional passive stiffness and load-independent contractility as indexed by the tissue active tension were optimized so that simulation results matched the measurements. The optimized parameters were compared with clinical metrics to find usable indicators associated with the underlying mechanical changes. Peak contractility of the RV free wall (RVFW) $\gamma_{RVFW,max}$ was found to be strongly correlated, and had an inverse relationship with the RV and left ventricle (LV) end-diastolic volume ratio (i.e., RVEDV/LVEDV) ($\gamma_{RVFW,max} = -0.13(\text{RVEDV/LVEDV})+0.44, R^2 = 0.77$). Correlation with RV ejection fraction ($R^2 = 0.50$) and end-diastolic volume index ($R^2 = 0.40$) were comparatively weaker. Patients with with RVEDV/LVEDV > 1.5 had 25% lower $\gamma_{RVFW,max}$ ($\text{P} < 0.05$) than that of the control. On average, RVFW passive stiffness increased progressively with the degree of remodeling as indexed by RVEDV/LVEDV. These results suggest a mechanical basis of using RVEDV/LVEDV as a clinical index for delineating disease severity and estimating RVFW contractility in PAH patients.

NEW AND NOTEWORTHY

Patient specific data assimilation of a patient cohort. Physical description of clinical observations.

I. INTRODUCTION

Pulmonary arterial hypertension (PAH) is a complex disorder caused by an increased vascular resistance in the pulmonary arterial circulatory system. As a consequence, pressure becomes elevated in the pulmonary artery and the right ventricle (RV). Unlike systemic

hypertension, PAH is difficult to detect in routine clinical examination, and the current gold standard for diagnosis is through invasive right heart catheterization[13]. Because of the difficulty in detecting PAH, the current estimated prevalence of this disease (15 to 50 per million) is most likely underestimated[39,40,43]. Perhaps also because of this difficulty, PAH is arguably less well-studied compared to systemic hypertension. Existing treatments largely are confined to relieving the symptoms and attenuating the disease progression[28]. As the disease progresses, the RV remodels both structurally and geometrically, becomes dysfunctional as a result, and eventually, this progression leads to decompensated heart failure and death.

A significant part of our current understanding of the ventricular mechanical alterations due to PAH has been developed using animal models[2,10,15,25,57], which may not fully reproduce the pathologies found in humans[53]. Human studies have so far been largely confined to measuring ventricular function of PAH patients at the global level[54]. Specifically, global RV contractility and wall stress are typically quantified using the maximal elastance (Emax)[12,41] and Laplace's law[46], respectively. However, the accuracy of Emax, defined as the maximum ratio of ventricular pressure to volume during the cardiac cycle, is highly dependent on the applied methodology. The gold standard for Emax estimation is through manipulation of venous return, but this is difficult to perform in practice[41]. Estimates in patients are often confined to single beat methods, for which the accuracy has been questioned[30,32]. Similarly, the use of Laplace's law is likely to be inaccurate when applied to the RV because of its irregular geometry[46]. On the other hand, while magnetic resonance (MR) and echo imaging can quantify regional (including RV) myocardial strain or motion *in vivo*[11,34,60], strain is a load-dependent quantity and not truly a measure of myocardial contractility. As described by Reichek[50], the popular notion of equating myocardial contractility with (load dependent) strain measures is "*off the mark [and] if contractility means anything, it is an expression of the ability of a given piece of myocardium to generate tension and shortening under any loading conditions*".

Computational modeling offers an opportunity to overcome these limitations through direct quantification of both passive and active ventricular mechanics under varying loading conditions. Such modeling has been heavily used to assess left ventricular dynamics, and a small number of computational modeling studies has been conducted to investigate alter-

ations of the RV mechanics in PAH[1,7,58]. These studies are, however, limited either by the use of non-human (rat) PAH data[7], the lack of consideration of patient-specific RV geometry[1], or the failure to take into account of the variability across PAH patients[58]. Consequently, there exists a gap in our current understanding on the changes in RV mechanics during the progression of PAH in humans. Here, we seek to narrow this gap by using a recently developed gradient-based data assimilation method[18] to evaluate patient-specific regional myocardial contractility and ventricular wall stresses from clinical PAH data. Specifically, we seek to answer the following three questions: First, is myocardial contractility, as indexed by the load-independent active tension generated by the tissue, altered in the left ventricular free wall (LVFW), right ventricular free wall (RVFW) and interventricular septum (SEPT) in PAH? Second, are ventricular wall stresses in the LV, septum, or in particularly in the RV, altered in PAH? Third, how are myocardial contractility and ventricular wall stresses associated with the progression of remodeling in PAH? We believe that answering these questions will help us to a better understanding the mechanical drivers of PAH progression, and contribute to optimization of existing treatment strategies and the development of new therapies.

II. METHODS

A. Patient Cohort and data processing

Twelve PAH patients were recruited in the study and underwent both cardiac magnetic resonance (CMR) scans and right heart catheterization (RHC) that were performed at rest using standard techniques. Pulmonary arterial hypertension was defined as having a mean pulmonary artery pressure (mPAP) greater than or equal to 25 mmHg with normal pulmonary capillary wedge pressure ($\leq$ 15 mmHg). The patients are from WHO group 1 (pulmonary arterial hypertension) with the majority associated with congenital heart disease. Six human subjects who had no known cardiovascular disease or other co-morbidities also underwent CMR scans and served as control in this study. Invasive hemodynamics measurements were not acquired in the control group. Demographics of the two study groups are summarized in Table I. The protocol was approved by the Local Institutional Review

Board, and informed consents were obtained from all subjects.

CMR imaging was performed using steady-state free precession (SSFP) cine gradient echo sequences. All subjects were imaged in a 3.0T Philips scanner (Philips-Adrglam; Philips Healthcare, Netherlands) with a 12-element body matrix coil. Steady state free precession end-expiratory breath-hold cine images were acquired in multi-planar short- and long-axis views. The typical imaging parameters were: TR/TE 34/1 ms, flip angle 45°, slice thickness 8 mm, echo time 1.404 ms, repetition time 2.808 ms, pixel bandwidth 1796 Hz, percent phase field of view 100 mm, temporal resolution 35 ms, in-plane spatial resolution 1.6 x 1.6 - 1.8 x 1.8 mm, 40 frame/cardiac cycle for the control group and 30 for the PAH group.

Left ventricular pressure was measured through arterial access by left heart catheterization, and RV pressure was measured by right heart catheterization. Continuous LV pressure, RV pressure waveforms and ECG signals were extracted from cath lab system and were aligned according to the simultaneously recorded ECG signals (R-R interval). These pressure waveforms were digitized using GetData Graph Digitizer (Version 2.26). A total of three consecutive heart cycles were averaged to deal with the respiratory artefact if any. Pressure-volume (PV) loops of the LV and RV of the PAH patients were then reconstructed by synchronizing the LV and RV pressure waveforms measured from catheterization and volume waveforms measured from the CMR images as described in Xi et al.[58]. Because the ventricular pressure waveforms were not acquired in the control subjects, pressure waveforms acquired from normal humans in previous studies were used as surrogate to synchronize with the measured volume waveforms to reconstruct the PV loops of each subject. Specifically, the mean normal RV pressure-waveform acquired from healthy human subjects in a previous study[49] was applied to all the control subjects. Based on a previous empirical study[29], a normal LV pressure-waveform with its end-systolic pressure scaled to be equal to 0.9 of the corresponding measured cuff pressure was applied to the control subjects. We have used this approach in our previous work[18,58].

Regional circumferential strain E_{cc} and longitudinal strain E_{ll} were estimated from the cine CMR images using a hyperelastic warping method, which has been used in previous studies to measure ventricular strains[22,23,44,55,60]. The hyperelastic warping method has also been evaluated and shown to produce good intra- and inter-observer agreement for estimating E_{cc} and E_{ll}[60]. Briefly, the biventricular geometry was segmented and reconstructed from

Variables	Control (n=6)	PAH (n=12)	P-value
Demographics			
Age, years old	52 ± 14	52 ± 11	0.989
Gender, Male/Female	1/5	2/10	0.755
Weight, kg	63.5 ± 16.9	61.2 ± 12.3	0.739
Height, cm	159 ± 8	161 ± 10	0.680
Clinical Exam			
Body surface area, m2	1.67 ± 0.25	1.65 ± 0.20	0.873
Body mass index, kg/m2	24.9 ± 4.0	23.6 ± 3.8	0.526
6 mins walking test, m	N/A	326 ± 134	N/A
NT-ProBNP, pg/mL	N/A	1188 ± 715	N/A
NYHA functional class I	N/A	1	N/A
NYHA functional class II	N/A	8	N/A
NYHA functional class III	N/A	3	N/A
NYHA functional class IV	N/A	0	N/A
Cardiac magnetic resonance			
LV ejection fraction, %	73 ± 7	58 ± 12	0.014
LVEDV, ml	93 ± 7	86 ± 30	0.574
LVESV, ml	25 ± 6	37 ± 21	0.198
LVSV, ml	68 ± 7	49 ± 14	0.009
LVFW ES wall thickness, mm	10.02 ± 1.25	10.87 ± 1.96	0.353
LVFW ED wall thickness, mm	5.42 ± 0.67	6.43 ± 1.29	0.093
RV ejection fraction, %	54 ± 11	37 ± 14	0.020
RVEDV, ml	103 ± 13	134 ± 72	0.322
RVESV, ml	47 ± 12	91 ± 68	0.148
RVSV, ml	56 ± 14	43 ± 13	0.095
RVFW ES wall thickness, mm	2.77 ± 0.24	6.22 ± 1.88	< 0.001
RVFW ED wall thickness, mm	1.75 ± 0.17	3.83 ± 0.61	< 0.001
Septum ES wall thickness, mm	9.21 ± 2.49	9.09 ± 2.75	0.926
Septum ED wall thickness, mm	6.13 ± 1.70	6.83 ± 2.20	0.508
Hemodynamics			
Heart rate, bpm	78 ± 16	88 ± 15	0.216
Diastolic blood pressure, mmHg	81 ± 15	75 ± 14	0.397
Systolic blood pressure, mmHg	140 ± 19	122 ± 27	0.170
Peak LV pressure, mmHg	N/A	129 ± 16	N/A
Peak RV pressure, mmHg	N/A	64 ± 15	N/A
LV end-diastolic pressure, mmHg	N/A	15 ± 2	N/A
RV end-diastolic pressure, mmHg	N/A	11 ± 5	N/A
LV max dPdt (mmHg/s)	N/A	1245 ± 309	N/A
LV min dPdt (mmHg/s)	N/A	-1295 ± 275	N/A
RV max dPdt (mmHg/s)	N/A	444 ± 273	N/A
RV min dPdt (mmHg/s)	N/A	-539 ± 232	N/A
Cardiac output, L/min	4.90 ± 1.16	3.98 ± 1.51	0.211
Cardiac index, L/min/m2	2.94 ± 0.57	2.39 ± 0.84	0.167
Right atrial pressure, mmHg	N/A	9 ± 9	N/A
Mean pulmonary artery pressure, mmHg	N/A	39 ± 9	N/A
Pulmonary capillary wedge pressure, mmHg	N/A	11 ± 3	N/A
Systemic vascular resistance, dyne s/cm5	N/A	1889 ± 751	N/A
Pulmonary vascular resistance, dyne s/cm5	N/A	535 ± 254	N/A
Pulmonary systemic flow ratio	N/A	0.33 ± 0.15	N/A
Pulmonary and systemic resistance ratio	N/A	0.99 ± 0.1	N/A

TABLE I: Demographics of the PAH patient and control groups

the cine CMR images using MeVisLab (http://www.mevislab.de). The geometry was then partitioned into 3 regions consisting of the LVFW, RVFW and SEPT[18,60]. The hyperelastic warping method was then applied to deform the reconstructed biventricular geometry from the template image into alignment with the corresponding object in the target image[22,23]. Normal strains in the circumferential and longitudinal directions at the LVFW, SEPT and RVFW regions were computed from the displacement field using end-diastole as the reference configuration. The circumferential and longitudinal directions in the biventricular unit were prescribed using a rule based algorithm[8].

B. Construction of Personalized Models

Personalized computational models of biventricular mechanics that fit the corresponding patient's pressure, volume, and regional strain data were created using previously described methods[18]. Briefly, the computational models were formulated based on classical large-deformation solid mechanics, and active contraction of the ventricular wall was incorporated by a multiplicative decomposition of the deformation gradient[6] :

$$\mathbf{F} = \mathbf{F}_e\mathbf{F}_a. \tag{1}$$

Here, $\mathbf{F} = \mathbf{I}+\nabla\mathbf{U}$ is the total deformation gradient computed from the displacement field $\mathbf{U}$, $\mathbf{F}_a$ is associated with an inelastic deformation resulting from the actively contracting muscle fibers, and $\mathbf{F}_e = \mathbf{F}\mathbf{F}_a^{-1}$ is associated with the elastic deformation that preserves (kinematic) compatibility of the tissue under load. We employ the following form of $\mathbf{F}_a$;

$$\mathbf{F}_a = (1-\gamma)\mathbf{f}_0 \otimes \mathbf{f}_0 + \frac{1}{\sqrt{1-\gamma}}(\mathbf{I} - \mathbf{f}_0 \otimes \mathbf{f}_0), \tag{2}$$

where $\mathbf{f}_0$ is the unit fiber direction in the reference configuration, and γ is a parameter that represents the relative active shortening strain along the muscle fibers i.e., a measure of the local load independent active tension generated by the tissue. Meanwhile, passive mechanics was modeled using a purely incompressible transversely isotropic hyperelastic material law[26] with an isochoric strain energy density given by

$$\Psi(\mathbf{C}_e) = \frac{a}{2b}\left(e^{b(I_1^E-3)} - 1\right) + \frac{a_f}{2b_f}\left(e^{b_f(I_{4\mathbf{f}_0}^E-1)_+^2} - 1\right), \tag{3}$$

where a, b, a_f, b_f are material constants and $I_1^E, I_{4\mathbf{f}_0}^E$ are reduced (pseudo-)invariants that are defined as

$$I_1^E = \mathrm{tr}\,\bar{\mathbf{C}}_e, \quad I_{4\mathbf{f}_0}^E = \mathbf{f}_0 \cdot (\bar{\mathbf{C}}_e \mathbf{f}_0), \tag{4}$$

with $\bar{\mathbf{C}}_e = J_e^{-\frac{2}{3}} \mathbf{C}_e$ being the volume preserving contribution to the elastic component of the right Cauchy Green strain tensor $\mathbf{C}_e = \mathbf{F}_e^T \mathbf{F}_e$, and $J_e = \det(\mathbf{F}_e)$ being the elastic volumetric deformation.

The ventricular base was fixed in the longitudinal direction and the biventricular geometry was anchored by constraining the epicardial surface using a Robin-type boundary condition with a linear spring of stiffness $k = 0.5$ kPa/cm[58]. We note that these constraints still allow for apical - basal shortening in the simulations. Measured cavity pressure in the LV (p_{lv}) and RV (p_{rv}) were applied as Neumann conditions at the endocardial surfaces. The force-balance equations were solved using the finite element method implemented in FEniCS[36]. A mixed formulation was used to enforce incompressibility of the elastic deformation ($J_e = 1$)[26]. Model results were tested for significance using Student t-tests with a chosen alpha value of 0.05. Statistical power was computed for selected results to test the effects of the low sample size on the findings.

In order to separately determine the active and passive material properties of the computational model for each patient, the clinical measurements were divided into a passive phase and an active phase. Models were then optimized using the active and passive material parameters as control variables to minimize a weighted cost function based on the differences between model predictions and measurements of pressure, volume and circumferential strain, E_{cc}, data as described previously[17,18]. Longitudinal strains were not included in the optimization due to the limited number of control parameters in the simulations, but served as an independent measure of the final model fit as in our previous study[18]. To solve the minimization problem, we applied a sequential quadratic programming algorithm (SQP)[31], which is a gradient-based optimization algorithm that requires the functional gradient of the cost function with respect to all the control variables. These gradients were estimated efficiently by solving an automatically derived adjoint equation using dolfin-adjoint[16].

In the passive phase of the optimization, we used the parameter a in Eq. (3) as a control variable, allowing this parameter to vary while keeping all other parameters fixed.

The parameter a scales the isotropic component of the transversely isotropic strain-energy function, and thereby characterizes the overall stiffness of the cardiac tissue. To capture regional differences in tissue stiffness, we introduce two different values of a; one associated with the LV (LVFW + SEPT, a_{LV}) and one with the RVFW (a_{RVFW}). These two parameters were allowed to vary independently from each other in the optimization. Similar to the procedure in Finsberg et al.[18], we first apply one iteration of the backward displacement method[9] to estimate an unloaded, stress-free configuration of the ventricles, thus neglecting residual stresses[21]. The passive parameter was then determined by assimilating the passive phase measurements, starting from an initial guess of $a_{LV} = a_{RVFW} = 1.291$kPa. After fitting the model to the passive phase of the PV-curve and strain data, the parameters a_{LV} and a_{RVFW} were held fixed and the relative active fiber shortening strain γ in Eq. (2) was chosen as the control variable for the active phase. While the chosen optimization method would in principle allow efficient estimation of any number of parameters, see[18], the fact that the passive parameters are constant while the active parameters are time dependent motivates the two-step optimization procedure. We allowed γ associated with the LVFW (γ_{LVFW}), SEPT (γ_{SEPT}) and RVFW (γ_{RVFW}) to vary independently from each other in order to capture of their spatial timing associated with active contraction. For each time point, we estimated γ_{LVFW}, γ_{SEPT} and γ_{RVFW}, to obtain their variation with time over a cardiac cycle. The spatially resolved isotropic parameters a and γ-waveforms were estimated with different linear transmural variation of the myofiber helix angles varying from $-\alpha$ at the epicardium to $+\alpha$ at the endocardium, with α ranging from 30° to 80°[18]. The set of parameters yielding the lowest mean square error between the predicted and measured strain and PV data was taken to be the optimal one and used to post-process regional biventricular myofiber wall stresses σ_{ff}.

III. RESULTS

A. Patient data and regional strains

The control and PAH groups have comparable demographic characteristics, with the majority of the patients in the latter group (8/12) classified in NYHA functional class II. In terms of hemodynamics, the PAH group had an mPAP of 39 ± 9 mmHg with a pulmonary

capillary wedge pressure (PCWP) 11 ± 3 mmHg. No differences in the systemic hemodynamics measurements (i.e., blood pressure) were detected between the 2 groups.

Evaluation of CMR images revealed that the PAH group had significantly ($P < 0.05$) reduced right ventricular ejection fraction (RVEF) ($37 \pm 14\%$ vs. $54 \pm 11\%$), increased RVFW thickness at ED (3.83 ± 0.61mm vs. 1.75 ± 0.17mm) and ES (6.22 ± 1.88mm vs. 2.27 ± 0.24mm) compared to the control group. Left ventricular ejection fraction (LVEF) and stroke volume (LVSV) were also significantly reduced in the PAH group compared to the control group (LVEF: $58 \pm 12\%$ vs. $73 \pm 7\%$; LVSV: 49 ± 14 ml vs. 68 ± 7 ml). Right ventricular end diastolic volume (RVEDV) and right ventricular end systolic volume (RVESV) were larger, but not statistically significant, in the PAH group. Although LV function, indexed by EF and SV, was significantly reduced in the patient group compared to the controls, only two of the patients were characterized with reduced ejection fraction (LVEF<50%).

Absolute peak circumferential strain E_{cc} in the PAH group was significantly lower (one-tailed: $P < 0.05$) than the control group at the LVFW ($13 \pm 4\%$ vs. $17 \pm 2\%$) and RVFW ($8 \pm 4\%$ vs. $11 \pm 2\%$) (Fig 1). Similarly, peak longitudinal strain E_{ll} in the PAH group was also significantly lower at the LVFW ($13 \pm 5\%$ vs. $17 \pm 3\%$) and RVFW ($10 \pm 4\%$ vs. $15 \pm 3\%$) compared to the control group. While both E_{cc} and E_{ll} at the septum were lower in the PAH group than the control group, these reductions were not statistically significant (one-tailed P = 0.11 for E_{cc} and 0.05 for E_{ll}).

B. Model results and validation

Optimized models were compared to measurements of cardiac volumes and strains for validation. For all cases, good temporal matching for pressure and volume was obtained, with Figure 2 showing the simulated pressure and volume traces against measurements for all cases.

The overall fit of the LV and RV volumes in the patient-specific computational models is very good, with the simulation results agreeing closely with the measurements in the cardiac cycle (Fig. 3). The overall root mean square error (RMSE) of the fit is 3.89 mL for the RV and 6.6 mL for the LV. Compared to the volumes, the fit of the regional strains in

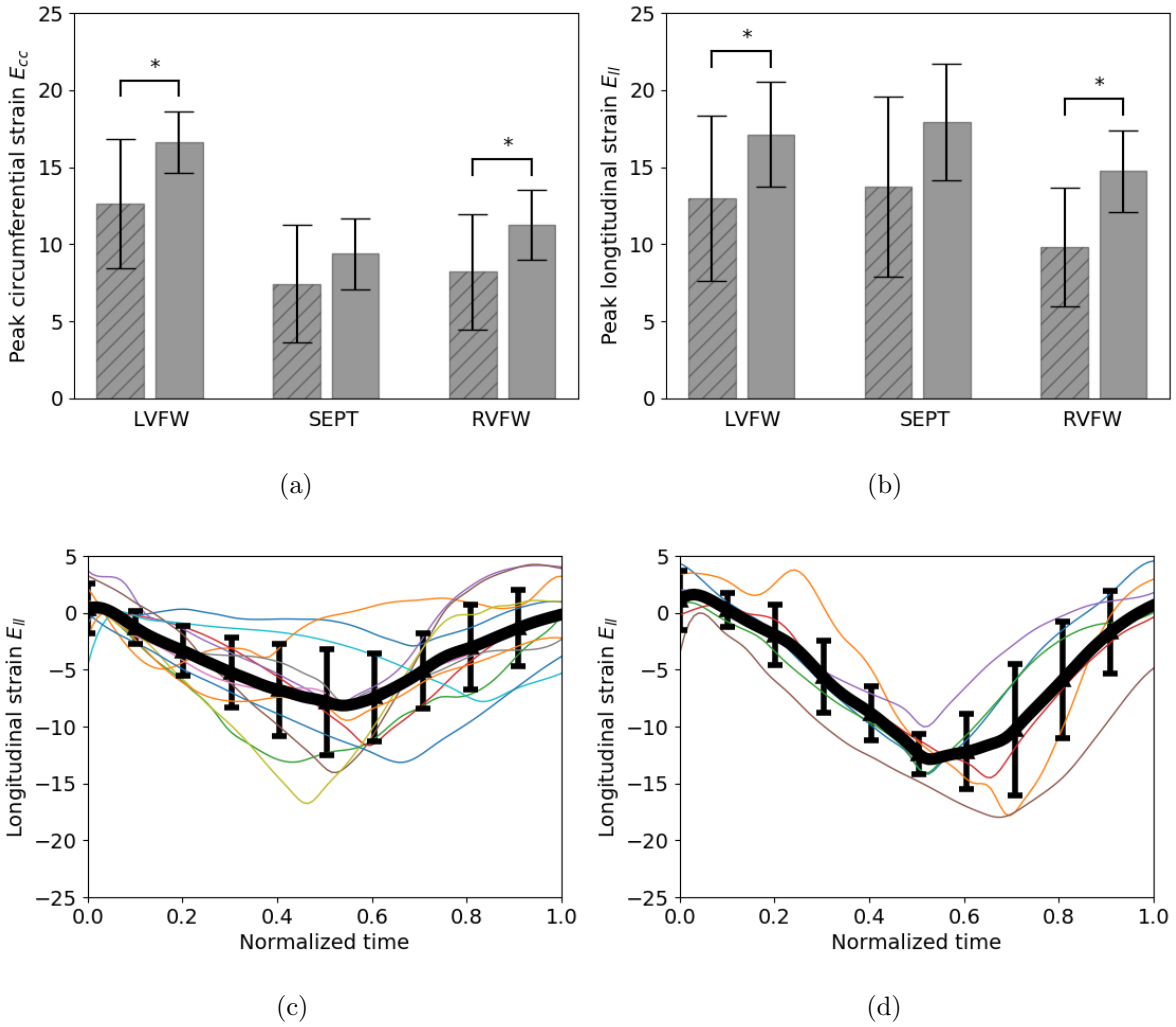

FIG. 1: Comparison of peak regional (a) circumferential and (b) longitudinal strains between control (unstriped) and PAH (striped) groups with (*) denoting that the latter value is statistically lower ($P < 0.05$) than the former. Time traces of RVFW longitudinal strain of the (c) PAH patients and (d) control subjects. Thick line denotes average and error bar denotes standard deviation.

the cardiac cycle shows significantly more scatter, especially at lower LV systolic strains. The RMSEs of the regional circumferential strain fit are 4.7% for the LVFW, 1.9% for the SEPT, and 2.6% for the RVFW. Meanwhile, serving as an independent measure of model fit, model prediction of longitudinal strains, which were not included in the optimization, have an RMSE of 6.2% for the LVFW, 6.2% for the SEPT, and 5.2% for the RVFW when

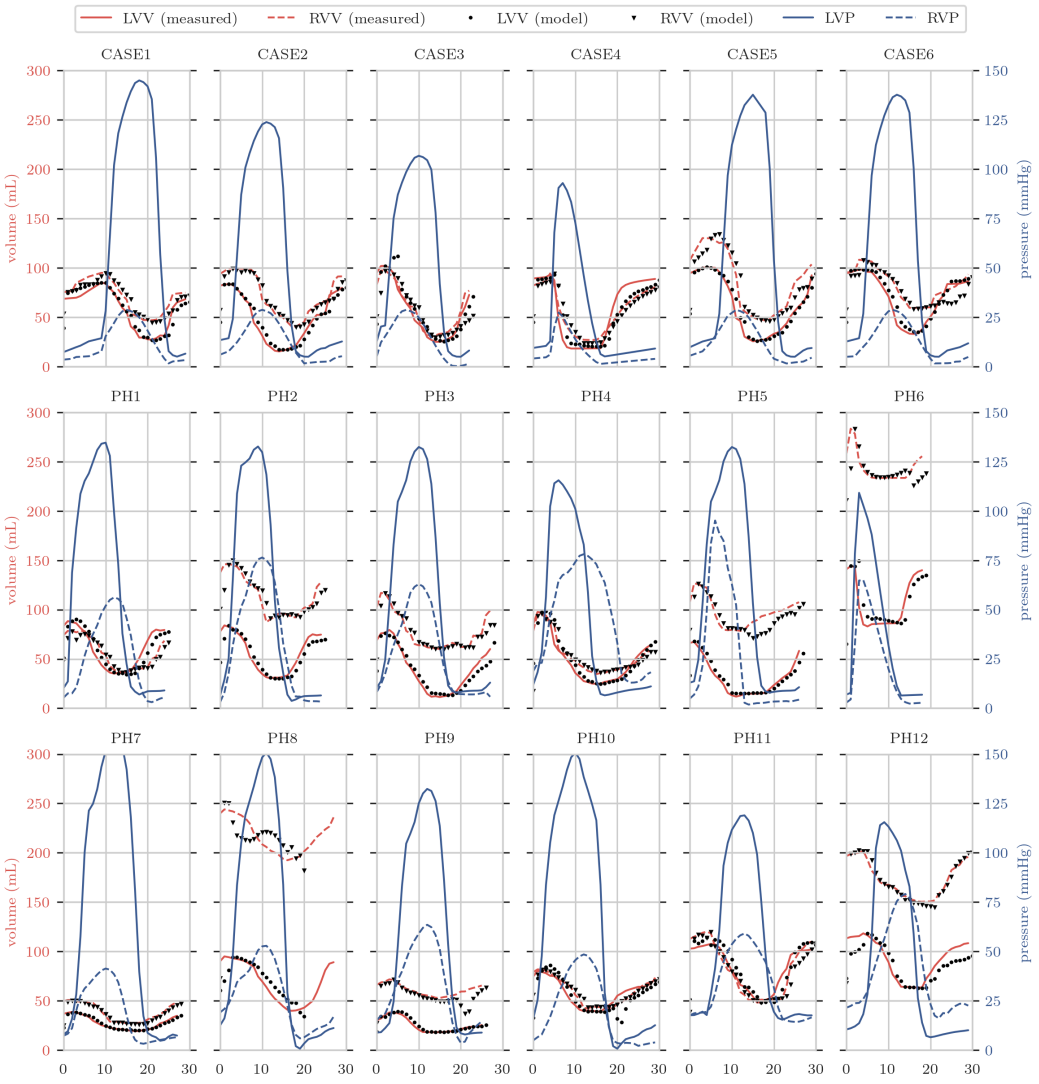

FIG. 2: Pressure (blue) and volume (red) traces for all simulations. Solid pressure lines give loading conditions for the simulations, while solid red lines show measured volumes of the ventricles. Dots indicate optimized simulated volumes for the time points.

compared with the measurements.

Figure 4 shows a comparison of model results for a single PAH patient and a healthy control. The figure illustrates the differences observed in the PAH group, including a shifted PV loop of the RV, increased LV diastolic stress and RV systolic stress, and significant thickening of the RV. Note that the particular cross section shown in the figure tends to exaggerate the extent of RV wall thickening. The average RVFW thickness in PAH patients was about two thirds of the septal thickness, compared to about one third in the controls

(Table I).

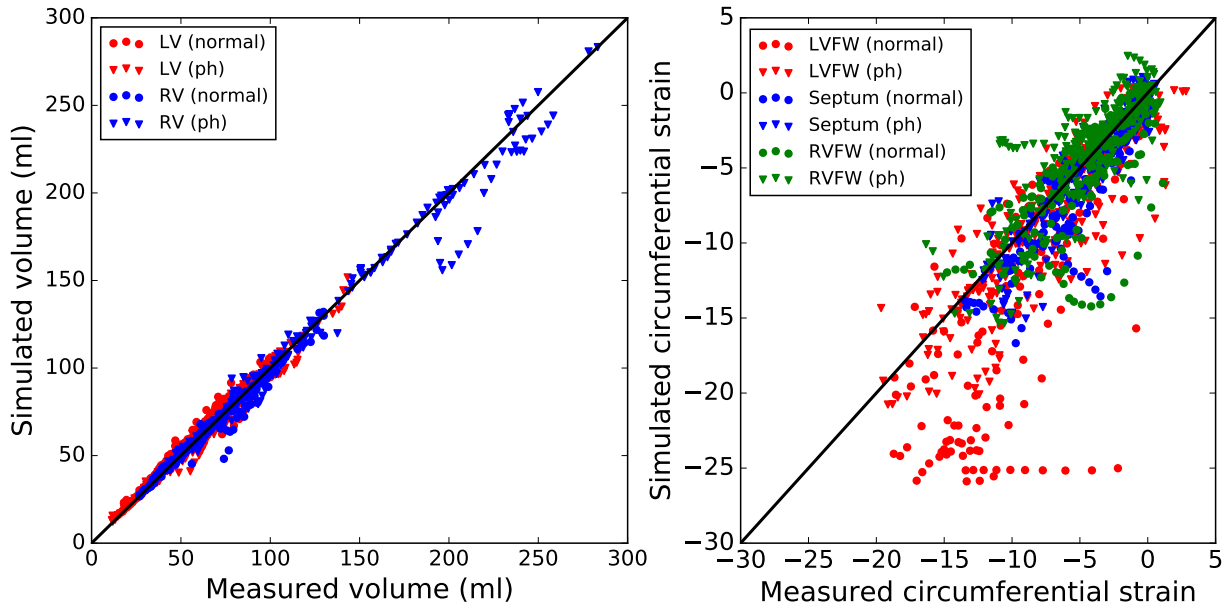

(a) (b)

FIG. 3: Overall data assimilation errors in the control (circle) and PAH patient (diamond) populations. Comparison between measured and simulated (a) volumes for both the RV (blue) and LV (red); (b) E_{cc} for the LVFW (red), SEPT (green), and RVFW (blue) at all cardiac time points. A $y = x$ line is also plotted to show the zero error reference.

C. Model results; contractility, stiffness, and stress

Regional contractility for the biventricular units was estimated using fitted values of the corresponding regional active strains $\gamma_{LVFW}, \gamma_{RVFW}, \gamma_{SEPT}$ during systole. Peak RVFW contractility $\gamma_{RVFW,max}$ is not uniformly decreased in the PAH group, but instead presented a pattern with respect to the level of remodeling (Fig 5). Using the ratio of RVEDV to LVEDV (i.e., RVEDV/LVEDV) as an indicator of remodeling, we found that RVEDV/LVEDV varies substantially in the PAH group (1.55 ± 0.50) but little in the control group (1.11 ± 0.12). With RVEDV/LVEDV $= 1.5$ (that is 3 SD from the mean value of the control group) serving as a threshold to delineate between PAH patients with mild RV remodeling (RVEDV/LVEDV < 1.5) and those with severe RV remodeling (RVEDV/LVEDV ≥ 1.5), we found that in

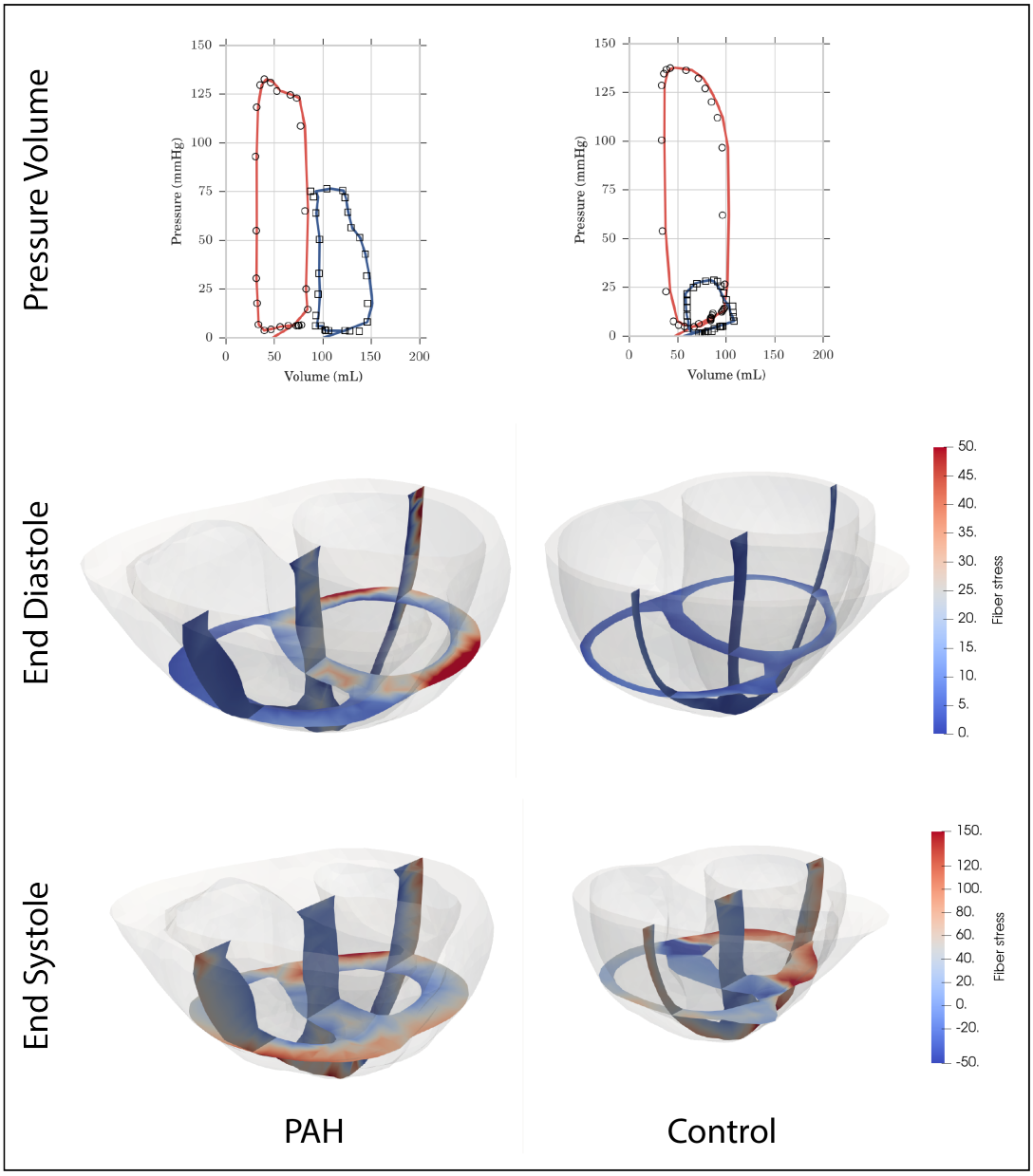

(a)

FIG. 4: Examples of simulation results from an extensively remodeled pulmonary hypertension patient, RVDEV/LVEDV = 1.75, (left column) and a healthy control (right column). A) PV loop data (open markers) and simulations (solid lines) for the LV (red) and RV (blue). B) Calculated fiber stresses at end diastole, and C) Calculated fiber stresses at end systole.

PAH patients with mild RV remodeling, their peak RVFW contractility $\gamma_{RVFW,max}$ is not

significantly changed compared to the control group (P = 0.09). We note that the threshold RVEDV/LVEDV = 1.5 is approximately the midpoint for the range (1.27 $\leq$ RVEDV/LVEDV $\leq$ 1.69) proposed previously[5] to categorize "mild" RV dilation in PAH patients. With increasing RVEDV/LVEDV, however, $\gamma_{RVFW,max}$ decreases linearly so that $\gamma_{RVFW,max}$ in PAH patients with RVEDV/LVEDV $\geq$ 1.5 (severely remodeled PAH) is significantly less than that in the control group. The inverse linear relationship between $\gamma_{RVFW,max}$ and RVEDV/LVEDV is strong and has a coefficient of determination $R^2 = 0.77$. By comparison, $\gamma_{RVFW,max}$ has a weaker linear relationship with RVEF ($R^2 = 0.50$) and RVEDV index (RVEDVi) ($R^2 = 0.40$).

Peak contractility in the LVFW $\gamma_{LVFW,max}$, unlike $\gamma_{RVFW,max}$, did not exhibit any relationship with the level of remodeling as measured by RVEDV/LVEDV (Fig 6). Specifically, we found that peak contractility in the LVFW $\gamma_{LVFW,max}$ is significantly smaller in the mildly remodeled PAH group with RVEDV/LVEDV < 1.5 (0.33 ± 0.02) compared to the control (0.38 ± 0.03) ($P < 0.05$). On the other hand, while the average $\gamma_{LVFW,max}$ in the severely remodeled PAH group (0.33 ± 0.07) is decreased compared to the control group, that decrease is not statistically significant, possibly due to high standard deviation and low sample size ($P = 0.14$, power = 0.35).

Fitted values of the regional material isotropic parameters a_{LV} and a_{RVFW} are measures of the tissue passive stiffness in the LVFW+SEPT and RVFW of the biventricular unit, respectively. Separating the fitted values in the PAH group based on the degree of remodeling (i.e., RVEDV/LVEDV) revealed a progressive increase in the mean value of a_{LV} and a_{RVFW} with remodeling (Fig. 7). The value a_{RVFW} of one patient in the severely remodeled PAH group (RVEDV/LVEDV $\geq$ 1.5) is disregarded as it appears to be an outlier (Z score > 2, $a = 36.78$kPa). In the severely remodeled PAH group, the mean value of a_{RVFW} (4.3 ± 3.5 kPa) is 2.4 times higher than that of the control group (1.8 ± 0.6 kPa) but that increase is not significant, possibly due to the large standard deviation and low sample size in the former group (power = 0.34). On the other hand, the mean value of a_{LV} in the severely remodeled PAH group (3.00 ± 2.5 kPa) is significantly higher (P < 0.05) than that of the control (0.48 ± 0.12 kPa).

Using the data-assimilated computational models, we computed the peak regional wall stress in the myofiber direction ($\sigma_{ff_{max}}$) (i.e., maximum myofiber load) (Fig. 8). We found

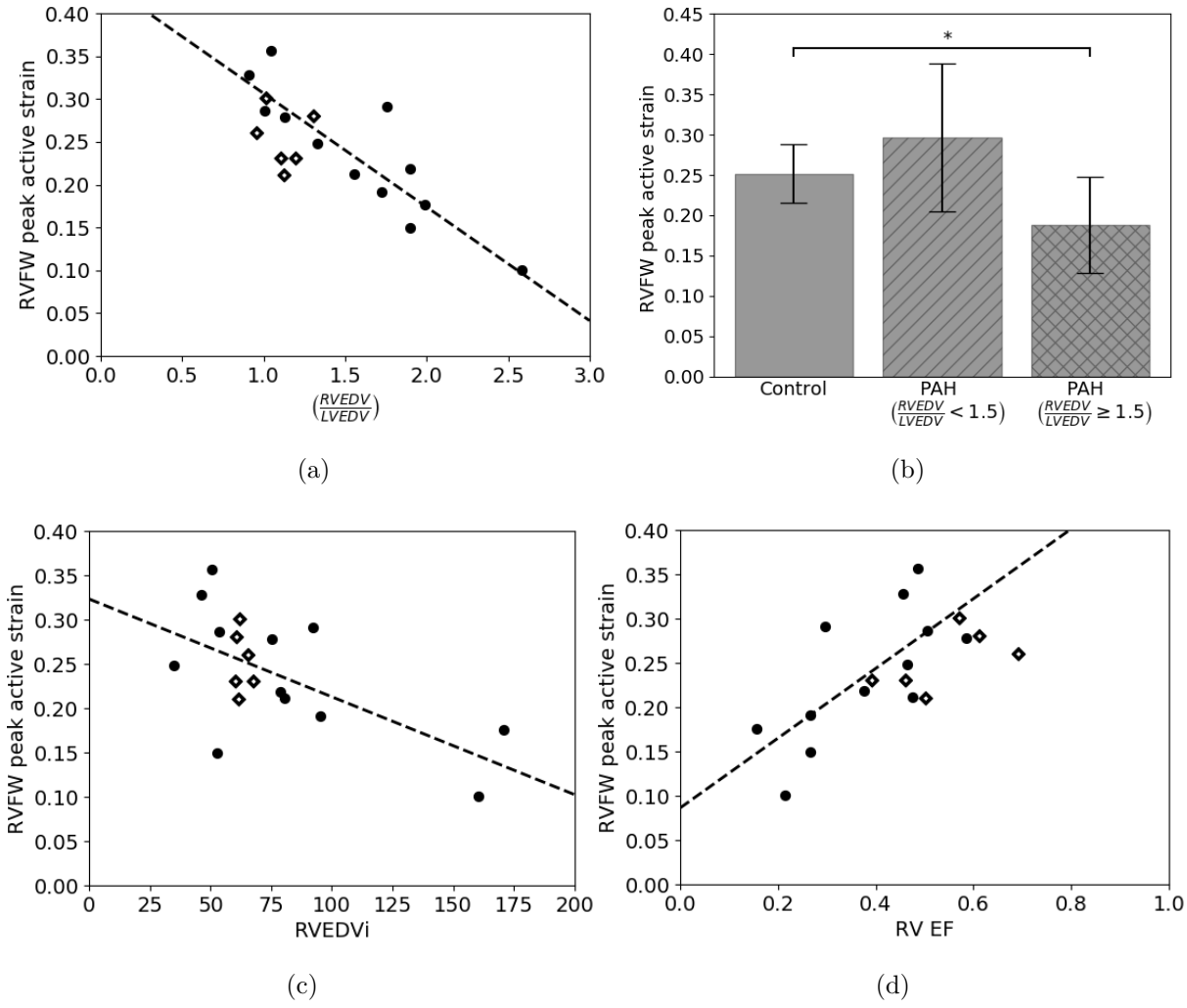

FIG. 5: Analysis of peak RVFW contractility $\gamma_{RVFW,max}$ for control and PAH patient groups. (a) Graphical depiction of $\gamma_{RVFW,max}$ for both controls (diamonds) and patients (black dots) as a function of the ratio of RVEDV/LVEDV. Dashed line shows a linear fit to the PAH patient group ($\gamma_{RVFW,max} = -0.13(\text{RVEDV/LVEDV})+0.44, R^2 = 0.77$). (b) Average $\gamma_{RVFW,max}$ for controls, patients with RVEDV/LVEDV < 1.5 and patients with RVEDV/LVEDV ≥ 1.5. (c) Linear fit of $\gamma_{RVFW,max}$ with RVEDVi ($\gamma_{RVFW,max} = -0.001(\text{RVEDVi})+0.32, R^2 = 0.40$) (d) Linear fit of $\gamma_{RVFW,max}$ with RVEF ($\gamma_{RVFW,max} = 0.39(\text{RVEF})+0.09, R^2 = 0.50$).

that $\sigma_{ff_{max}}$ at the RVFW is, on average, the same between the the control (36.4 $\pm$ 5.7 kPa) and the mildly remodeled PAH (36.5 $\pm$ 12 kPa) groups. In the severely remodeled PAH group, however, $\sigma_{ff_{max}}$ at the RVFW is on average 1.5 times larger (54.27 $\pm$ 25.1 kPa) than

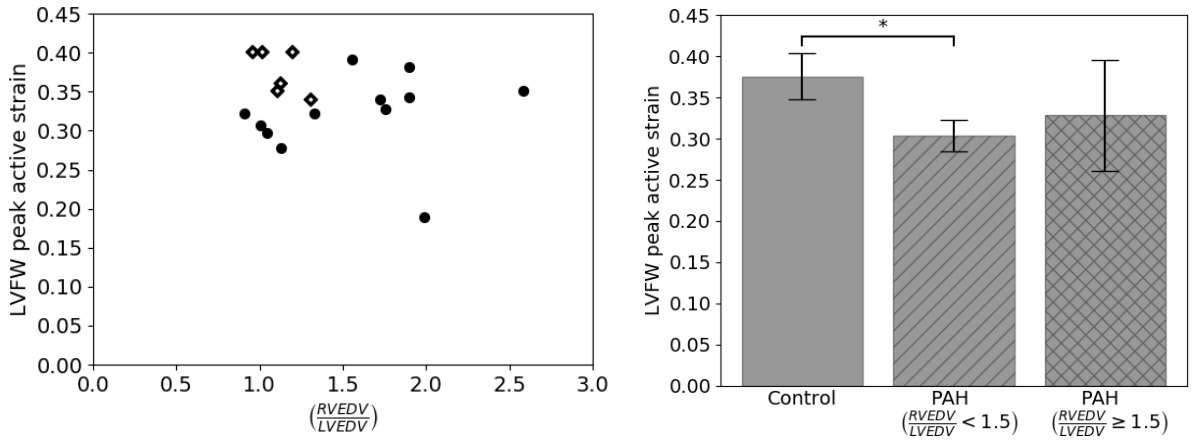

(a) (b)

FIG. 6: Analysis of peak LVFW contractility $\gamma_{LVFW,max}$ for control and PAH patient groups. (a) Graphical depiction of peak LVFW contractility for both controls (diamonds) and patients (black dots) as a function of RVEDV/LVEDV. (b) Average $\gamma_{LVFW,max}$ for controls, patients with RVEDV/LVEDV < 1.5 and patients with RVEDV/LVEDV ≥ 1.5.

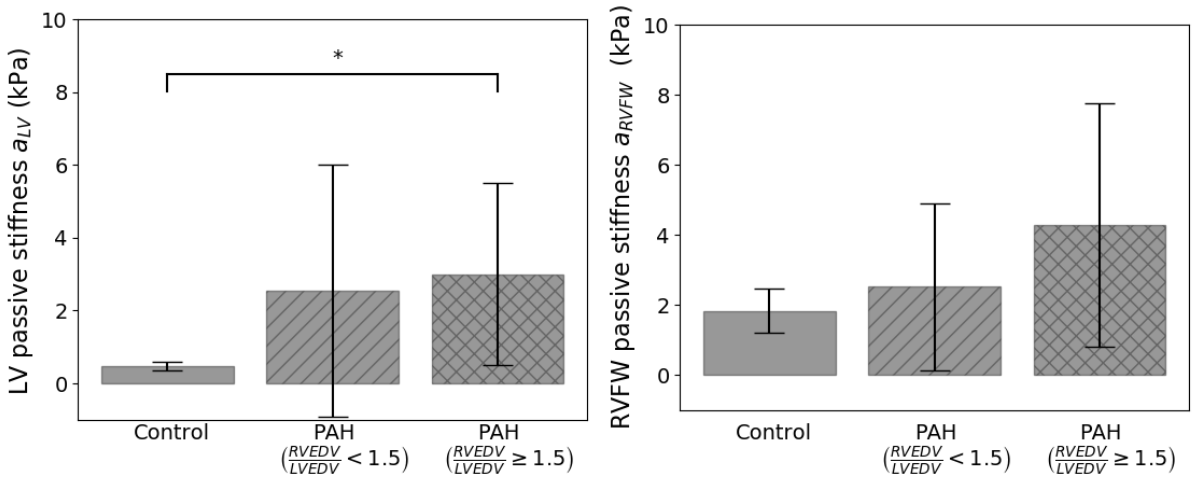

(a) (b)

FIG. 7: Comparison of passive tissue stiffness parameter a between control and the PAH groups in the (a) LVFW + SEPT and (b) RVFW regions

these 2 groups, but that difference is not significant ($P = 0.14$, power $= 0.33$) due to its large standard deviation. In comparison, $\sigma_{ff_{max}}$ at the LVFW is significantly reduced in the mildly remodeled PAH group (55.4 $\pm$ 7.4 kPa) compared to the control group (84 $\pm$

17.6 kPa). In the severely remodeled PAH group, $\sigma_{ff_{max}}$ at the LVFW of two patients are disregarded as they appeared to be outliers with substantially large values (Z score > 2, $\sigma_{ff_{max}} = 544.1, 1659.9$ kPa), which is due likely to the presence of local stress-concentration in the model. Peak myofiber stress $\sigma_{ff_{max}}$ at the LVFW in this group (71.22 ± 7.8 kPa) is significantly larger than the mildly remodeled PAH group but lower (not statistically significant) than the control.

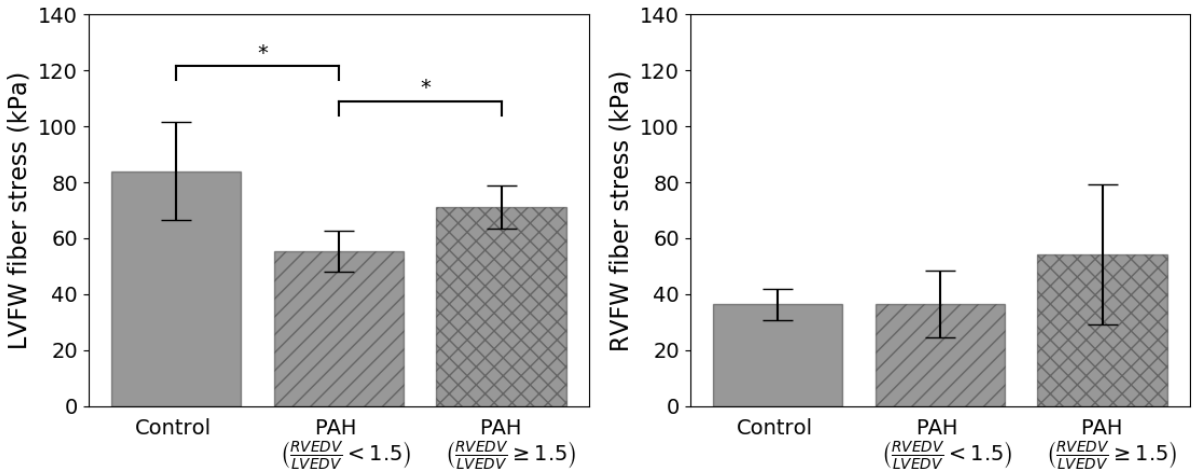

(a) (b)

FIG. 8: Comparison of peak myofiber wall stress $\sigma_{ff_{max}}$ between control and the PAH groups in the (a) LVFW and (b) RVFW regions.

IV. DISCUSSION

We have used a previously established data assimilation technique[17,18] to quantify changes in regional myocardial properties and stresses in PAH based on measurements of PV loops and myocardial strains from patients and a cohort of healthy subjects serving as control. The major finding of this study is a strong inverse linear relationship between the RVFW load-independent contractility, as indexed by the fitted model's active strain parameter $\gamma_{RVFW,max}$, and the degree of remodeling as indexed by RVEDV/LVEDV in PAH patients. We have previously suggested that the contractility parameter $\gamma_{RVFW,max}$ could possibly be a biomarker of ventricular failure[17], and its relationship to RVEDV/LVEDV ($R^2 = 0.77$) is stronger than that with RVEF ($R^2 = 0.50$) or RVEDVi ($R^2 = 0.40$) in PAH patients. We also

found that RVFW contractility is increased by about 20% in the PAH patients when little remodeling is present (i.e., RVEDV/LVEDV < 1.5), but decreases linearly with increasing RVEDV/LVEDV.

The strong $\gamma_{RVFW,max}$–RVEDV/LVEDV relationship also suggest a mechanistic explanation for recent clinical findings that RVEDV/LVEDV is a better metric (with a higher sensitivity) than RVEDVi for identifying PAH patients based on all-cause mortality[5] as well as for detecting RV enlargement[4]. Besides PAH, this metric is also used for assessing RV dilation and indicating pulmonary valve replacement in patients who have tetralogy of Fallot[19,35]. There is, however, no other clear mechanistic basis for applying RVEDV/LVEDV to delineate the severity of PAH or electing surgery, other than a statistical association of this metric with clinical endpoints[5] or from clinical experience[35]. Our finding suggests that the underlying reason why RVEDV/LVEDV is a better metric in determining PAH severity is because of its close association with RVFW contractility in PAH. Based on this relationship (Fig. 5a), the threshold of RVEDV/LVEDV ~ 2 for distinguishing PAH patients with severe RV dilation as well as electing patients for pulmonary valve replacement is associated with a reduction of RVFW contractility by about 30% from normal.

Fundamentally, our study also provides an insight into the changes in regional contractility during the progression of PAH. Our result suggests there is an increase in the RV contractility in early stages of PAH (RVEDV/LVEDV < 1.5), perhaps as a compensatory mechanism to maintain RVEF in response to the increased RV pressure, before it decreases as the disease progresses. The similarity in RVEF in PAH patients with RVEDV/LVEDV < 1.5 ($49 \pm 5\%$) compared to normal ($54 \pm 11\%$) (Fig. 5) support this theory. Because wall thickness is already accounted for geometrically in the computational models, the increase in RVFW contractility indicates that RV cardiomyocytes become hypercontractile in an attempt to normalize RVEF in the presence of increased pulmonary afterload at early stages of PAH. This finding is supported by a recent study, which shows that the maximal tension of skinned myocytes of idiopathic PAH patients is 28% higher than normal in early stages of disease with RVEF at $46 \pm 7\%$[27], close to that found in PAH patients with RVEDV/LVEDV < 1.5 in this study. Other than affecting the RV, we also found that LV contractility γ_{LVFW} in PAH patients is reduced. This reduction is observed even in PAH patients exhibiting little RV remodeling suggesting that there is some early influence on LV function in this disease,

a result broadly consistent with findings of reduced myocyte contractility in the LV of PAH patients[37].

Besides contractility, we found that there is, on average, an increase in the LV and RV passive stiffness (reflected by a_{LV}, a_{RVFW}) with increased RVEDV/LVEDV in the PAH groups. While this increase is largely not statistically significant, due to the large variance of the fitted parameter values, the result is consistent with experimental[47] and clinical[27] findings that PAH is associated with cardiac fibrosis and passive tissue stiffening. Interestingly, we also find that the peak LV fiber stress is reduced in PAH patients with mild RV remodeling but is relatively unchanged in those with severe RV remodeling compared to the controls. This result could be due to changes in LV dynamics associated with a change in passive tissue stiffening and septal loading. Computation of the peak RV fiber stress using the fitted parameters, on the other hand, revealed that it is increased only in the severely remodeled PAH patients, with RVEDV/LVEDV ≥ 1.5, although that increase is not statistically significant ($P = 0.14$, Fig. 8). Because myocardial wall stress is directly correlated with myocardial oxygen consumption (MVO2), this result suggests that MVO2 is increased in the RV of PAH patients with RVEDV/LVEDV ≥ 1.5 but less so in patients without substantial RV remodeling. When taken into account with our finding that RVFW contractility is reduced in PAH patients with RVEDV/LVEDV ≥ 1.5, this result further suggests that coronary flow may not be sufficient to meet the increase in MVO2 due to a higher workload in the RV, and as a result, ischemia sets in this cohort of patients producing a lower contractility. Our finding that RVEDV/LVEDV ≥ 1.5 may represent the threshold at which RV may become ischemic (with reduced contractility) is also consistent with clinical observations that RV ischemia may play a role in later stages of the disease[24,42].

Compared to previous patient data assimilation techniques that have so far been only applied to the LV[17,20,33,59] with a relatively small number of patients ($n \sim 6$), we have shown that the semi-automatic data assimilation pipeline when applied to the biventricular unit is robust in regards to a sizable patient cohort ($n = 12$) that has features reflecting those found in the general heterogeneous PAH population. Specifically, PAH patients recruited in this study had mPAP $= 39 \pm 9$ mmHg and PCWP $= 11 \pm 3$ mmHg, which falls within the clinical definition of this disease (mPAP ≥ 25 mmHg and PCWP < 15 mmHg)[38]. In terms of geometry and function, the PAH patients had thicker RV wall, higher mean RVEDV,

lower RV and LV EF as well as significantly reduced longitudinal and circumferential strains at the RVFW and LVFW that are all consistent with previous clinical observations of this disease[3,14,45,46,48,51,52]. The data assimilation process produces relatively few data outliers for both the control and patient groups, and is able to fit the patient-specific ventricular volumes and regional strains well, especially considering the fact that only a small number of control variables is used in fitting the data.

A. Limitations and future directions

Some limitations and challenges remain in regards to this study. One significant limitation is the lack of use of longitudinal strain data in the optimization, which resulted in relatively high error between the model and the measurements, especially in the septal region. We chose to use a minimal set of parameters in the optimization to prevent over fitting and to best discern between patient groups, but inaccuracy in the model in these regions may produce errors in these estimates. While we are able to fit the PV loops and regional circumferential strains relatively well in this study, it will be useful to further explore the potential impact of the choice of the computational model and the control variables used to fit the patient data. This is particularly true in regards to chosen fiber angles. Although we saw little sensitivity to the overall results between using literature values and optimized fiber angles (see supplementary material), further study is needed to understand how best to incorporate variable fiber angles into patient specific simulations. At the same time, the choice of boundary conditions may also influence the results (see supplementary material) and further work is needed to determine the most appropriate boundary conditions to be used for this type of analysis. It should also be noted that longitudinal strains are correlated to the circumferential strains through the incompressibility condition, and therefore the validation is not as strong as it would have been using an independent observable. In addition, even with this connection, the absolute errors in the longitudinal strain remain relatively large in our simulations. Second, the cohort size ($n = 12$) is fairly small, although it is still larger than many other patient-specific computational modeling studies. This limited sample size, especially with the need to further refine the patient group by level of remodeling, creates a somewhat under-powered study to investigate all the mechanical

factors that could be important. Additional work is needed in larger cohorts to verify and refine some results, especially the relationship between LV and RV dynamics. For instance, our results indicated an increase in LV passive stiffness in PAH patients, which is consistent with previous experimental and clinical findings. A sensitivity analysis (see supplementary material) of passive stiffness to LV diastolic pressure further supports that the increase is not a modeling artefact but a real difference between the groups. However, because of the large variability of fitted parameter values the results are not statistically significant, and will need to be confirmed in a larger cohort. Nevertheless, we are able to suggest a broad mechanistic explanation as to why some clinical indices are better at characterizing PAH severity as well as features found during the progression of PAH, which are also supported by other clinical studies. A larger cohort will be considered in future studies. Third, we have applied surrogate pressure waveforms to the control subjects as RHC was not performed on them. Future studies can consider estimating pressures in control healthy subjects using doppler echocardiography or including human subjects who have had false-positive diagnosis of PAH after undergoing RHC. Lastly, although an active strain formulation is able to provide information on the contraction dynamics and relative twitch strength, it is difficult to contextualize these results against other studies based on the active stress framework. In the supplementary material, we show that essential properties such as the force-length relationship are captured by the formulation of active strain, but additional work is needed to link active strain dynamics with the more physiologically derived active stress frameworks. Detailed studies of this kind will be important for comparing our findings with other studies and standards, and would be particularly useful in optimizations that utilize dynamic information such as myofiber force generation over the entire twitch.

V. CONCLUSION

In conclusion, we have shown that RVEDV/LVEDV is strongly associated with the RVFW load-independent contractility estimated from assimilating a computational model of active biventricular mechanics with clinical imaging and hemodynamics data acquired from PAH patients and control subjects. Our study therefore suggests a mechanistic basis for using RVEDV/LVEDV as a non-invasive metric for assessing PAH severity as well as a non-invasive

approach of estimating RV contractility from measurements of RVEDV/LVEDV.

ACKNOWLEDGMENTS

This study was partially supported by Singapore Ministry of Health's National Medical Research Council Singapore (NMRC/OFIRG/0018/2016, Zhong), the Goh Cardiovascular Research Grant (Duke-NUS-GCR/2013/0009, Zhong), AHA SDG (17SDG33370110, Lee), NIH (R01-HL-134841, Lee), and the Center for Cardiological Innovation (Research Council of Norway)

SUPPLEMENTARY MATERIAL

Supplementary material can be found at https://doi.org/10.5281/zenodo.3357016

---

* These two authors contributed equally to the work

[1] Acosta, S., Puelz, C., Rivière, B., Penny, D. J., Brady, K. M., and Rusin, C. G. (2017). Cardiovascular mechanics in the early stages of pulmonary hypertension: a computational study. *Biomechanics and modeling in mechanobiology*, 16(6):2093–2112.

[2] Aguero, J., Ishikawa, K., Hadri, L., Santos-Gallego, C., Fish, K., Hammoudi, N., Chaanine, A., Torquato, S., Naim, C., Ibanez, B., et al. (2014). Characterization of right ventricular remodeling and failure in a chronic pulmonary hypertension model. *American Journal of Physiology-Heart and Circulatory Physiology*, 307(8):H1204–H1215.

[3] Altmayer, S. P., Losada, N., Patel, A. R., Addetia, K., Gomberg-Maitland, M., Forfia, P. R., and Han, Y. (2015). Cmr rv size assessment should include rv to lv volume ratio. *Journal of Cardiovascular Magnetic Resonance*, 17(1):P394.

[4] Altmayer, S. P., Patel, A. R., Addetia, K., Gomberg-Maitland, M., Forfia, P. R., and Han, Y. (2016). Cardiac mri right ventricle/left ventricle (rv/lv) volume ratio improves detection of rv enlargement. *Journal of Magnetic Resonance Imaging*, 43(6):1379–1385.

[5] Altmayer, S. P. L., Han, Q. J., Addetia, K., Patel, A. R., Forfia, P. R., and Han, Y. (2018). Using

all-cause mortality to define severe RV dilation with RV/LV volume ratio. *Scientific Reports*, 8(1):7200.

[6] Ambrosi, D., Arioli, G., Nobile, F., and Quarteroni, A. (2011). Electromechanical coupling in cardiac dynamics: the active strain approach. *SIAM Journal on Applied Mathematics*, 71(2):605–621.

[7] Avazmohammadi, R., Mendiola, E. A., Soares, J. S., Li, D. S., Chen, Z., Merchant, S., Hsu, E. W., Vanderslice, P., Dixon, R. A., and Sacks, M. S. (2018). A computational cardiac model for the adaptation to pulmonary arterial hypertension in the rat. *Annals of biomedical engineering*, pages 1–16.

[8] Bayer, J. D., Blake, R. C., Plank, G., and Trayanova, N. A. (2012). A novel rule-based algorithm for assigning myocardial fiber orientation to computational heart models. *Annals of biomedical engineering*, 40(10):2243–2254.

[9] Bols, J., Degroote, J., Trachet, B., Verhegghe, B., Segers, P., and Vierendeels, J. (2013). A computational method to assess the in vivo stresses and unloaded configuration of patient-specific blood vessels. *Journal of computational and Applied mathematics*, 246:10–17.

[10] Borgdorff, M. A., Bartelds, B., Dickinson, M. G., Steendijk, P., de Vroomen, M., and Berger, R. M. (2013). Distinct loading conditions reveal various patterns of right ventricular adaptation. *American Journal of Physiology-Heart and Circulatory Physiology*, 305(3):H354–H364.

[11] Bossone, E., D'andrea, A., D'alto, M., Citro, R., Argiento, P., Ferrara, F., Cittadini, A., Rubenfire, M., and Naeije, R. (2013). Echocardiography in pulmonary arterial hypertension: from diagnosis to prognosis. *Journal of the American Society of Echocardiography*, 26(1):1–14.

[12] Brown, K. A. and Ditchey, R. V. (1988). Human right ventricular end-systolic pressure-volume relation defined by maximal elastance. *Circulation*, 78(1):81–91.

[13] Champion, H. C., Michelakis, E. D., and Hassoun, P. M. (2009). Comprehensive invasive and noninvasive approach to the right ventricle–pulmonary circulation unit: state of the art and clinical and research implications. *Circulation*, 120(11):992–1007.

[14] de Amorim Corrêa, R., de Oliveira, F. B., Barbosa, M. M., Barbosa, J. A. A., Carvalho, T. S., Barreto, M. C., Campos, F. T. A. F., and Nunes, M. C. P. (2016). Left ventricular function in patients with pulmonary arterial hypertension: The role of two-dimensional speckle tracking strain. *Echocardiography*, 33(9):1326–1334.

[15] Faber, M. J., Dalinghaus, M., Lankhuizen, I. M., Steendijk, P., Hop, W. C., Schoemaker, R. G., Duncker, D. J., Lamers, J. M., and Helbing, W. A. (2006). Right and left ventricular function after chronic pulmonary artery banding in rats assessed with biventricular pressure-volume loops. *American Journal of Physiology-Heart and Circulatory Physiology*, 291(4):H1580–H1586.

[16] Farrell, P. E., Ham, D. A., Funke, S. W., and Rognes, M. E. (2013). Automated derivation of the adjoint of high-level transient finite element programs. *SIAM Journal on Scientific Computing*, 35(4):C369–C393.

[17] Finsberg, H., Balaban, G., Ross, S., Håland, T. F., Odland, H. H., Sundnes, J., and Wall, S. (2018a). Estimating cardiac contraction through high resolution data assimilation of a personalized mechanical model. *Journal of Computational Science*, 24:85 – 90.

[18] Finsberg, H., Xi, C., Tan, J. L., Zhong, L., Genet, M., Sundnes, J., Lee, L. C., and Wall, S. T. (2018b). Efficient estimation of personalized biventricular mechanical function employing gradient-based optimization. *International journal for numerical methods in biomedical engineering*, page e2982.

[19] Frigiola, A., Tsang, V., Bull, C., Coats, L., Khambadkone, S., Derrick, G., Mist, B., Walker, F., van Doorn, C., Bonhoeffer, P., et al. (2008). Biventricular response after pulmonary valve replacement for right ventricular outflow tract dysfunction: is age a predictor of outcome? *Circulation*, 118(14 suppl 1):S182–S190.

[20] Genet, M., Lee, L. C., Ge, L., Acevedo-Bolton, G., Jeung, N., Martin, A., Cambronero, N., Boyle, A., Yeghiazarians, Y., Kozerke, S., et al. (2015a). A novel method for quantifying smooth regional variations in myocardial contractility within an infarcted human left ventricle based on delay-enhanced magnetic resonance imaging. *Journal of biomechanical engineering*, 137(8):081009.

[21] Genet, M., Rausch, M., Lee, L. C., Choy, S., Zhao, X., Kassab, G. S., Kozerke, S., Guccione, J. M., and Kuhl, E. (2015b). Heterogeneous growth-induced prestrain in the heart. *Journal of biomechanics*, 48(10):2080–2089.

[22] Genet, M., Stoeck, C., Von Deuster, C., Lee, L., and Kozerke, S. (2018). Equilibrated warping: Finite element image registration with finite strain equilibrium gap regularization. *Medical image analysis*, 50:1–22.

[23] Genet, M., Stoeck, C., Von Deuster, C., Lee, L. C., Guccione, J., and Kozerke, S. (2016). Finite

element digital image correlation for cardiac strain analysis from 3d whole-heart tagging. In *ISMRM 24rd Annual Meeting and Exhibition 2016*.

[24] Gómez, A., Bialostozky, D., Zajarias, A., Santos, E., Palomar, A., Martínez, M. L., and Sandoval, J. (2001). Right ventricular ischemia in patients with primary pulmonary hypertension. *Journal of the American College of Cardiology*, 38(4):1137–1142.

[25] Hill, M. R., Simon, M. A., Valdez-Jasso, D., Zhang, W., Champion, H. C., and Sacks, M. S. (2014). Structural and mechanical adaptations of right ventricle free wall myocardium to pressure overload. *Annals of biomedical engineering*, 42(12):2451–2465.

[26] Holzapfel, G. A. and Ogden, R. W. (2009). Constitutive modelling of passive myocardium: a structurally based framework for material characterization. *Philosophical Transactions of the Royal Society of London A: Mathematical, Physical and Engineering Sciences*, 367(1902):3445–3475.

[27] Hsu, S., Kokkonen-Simon, K. M., Kirk, J. A., Kolb, T. M., Damico, R. L., Mathai, S. C., Mukherjee, M., Shah, A. A., Wigley, F. M., Margulies, K. B., et al. (2018). Right ventricular myofilament functional differences in humans with systemic sclerosis–associated versus idiopathic pulmonary arterial hypertension. *Circulation*, 137(22):2360–2370.

[28] Jais, X. and Bonnet, D. (2010). Treatment of pulmonary arterial hypertension. *Presse medicale (Paris, France: 1983)*, 39:1S22–32.

[29] Kelly, R. P., Ting, C.-T., Yang, T.-M., Liu, C.-P., Maughan, W. L., Chang, M.-S., and Kass, D. A. (1992). Effective arterial elastance as index of arterial vascular load in humans. *Circulation*, 86(2):513–521.

[30] Kjørstad, K. E., Korvald, C., and Myrmel, T. (2002). Pressure-volume-based single-beat estimations cannot predict left ventricular contractility in vivo. *American Journal of Physiology-Heart and Circulatory Physiology*, 282(5):H1739–H1750.

[31] Kraft, D. (1988). A software package for sequential quadratic programming. *Forschungsbericht-Deutsche Forschungs- und Versuchsanstalt fur Luft- und Raumfahrt*.

[32] Lambermont, B., Segers, P., Ghuysen, A., Tchana-Sato, V., Morimont, P., Dogne, J.-M., Kolh, P., Gerard, P., and D'orio, V. (2004). Comparison between single-beat and multiple-beat methods for estimation of right ventricular contractility. *Critical care medicine*, 32(9):1886–1890.

[33] Lee, L. C., Wenk, J. F., Klepach, D., Zhang, Z., Saloner, D., Wallace, A. W., Ge, L., Rat-

cliffe, M. B., and Guccione, J. M. (2011). A novel method for quantifying in-vivo regional left ventricular myocardial contractility in the border zone of a myocardial infarction. *Journal of biomechanical engineering*, 133(9):094506.

[34] Leng, S., Jiang, M., Zhao, X.-D., Allen, J. C., Kassab, G. S., Ouyang, R.-Z., Tan, J.-L., He, B., Tan, R.-S., and Zhong, L. (2016). Three-dimensional tricuspid annular motion analysis from cardiac magnetic resonance feature-tracking. *Annals of biomedical engineering*, 44(12):3522–3538.

[35] Lindsey, C. W., Parks, W. J., Kogon, B. E., Sallee III, D., and Mahle, W. T. (2010). Pulmonary valve replacement after tetralogy of fallot repair in preadolescent patients. *The Annals of thoracic surgery*, 89(1):147–151.

[36] Logg, A., Mardal, K.-A., and Wells, G. (2012). *Automated solution of differential equations by the finite element method: The FEniCS book*, volume 84. Springer Science & Business Media.

[37] Manders, E., Bogaard, H.-J., Handoko, M. L., van de Veerdonk, M. C., Keogh, A., Westerhof, N., Stienen, G. J., dos Remedios, C. G., Humbert, M., Dorfmüller, P., et al. (2014). Contractile dysfunction of left ventricular cardiomyocytes in patients with pulmonary arterial hypertension. *Journal of the American College of Cardiology*, 64(1):28–37.

[38] McLaughlin, V. V., Archer, S. L., Badesch, D. B., Barst, R. J., Farber, H. W., Lindner, J. R., Mathier, M. A., McGoon, M. D., Park, M. H., Rosenson, R. S., et al. (2009). A report of the american college of cardiology foundation task force on expert consensus documents and the american heart association. *Circulation*, 119(16):2250–2294.

[39] McLaughlin, V. V. and McGoon, M. D. (2006). Pulmonary arterial hypertension. *Circulation*, 114(13):1417–1431.

[40] Mocumbi, A. O., Thienemann, F., and Sliwa, K. (2015). A global perspective on the epidemiology of pulmonary hypertension. *Canadian Journal of Cardiology*, 31(4):375–381.

[41] Naeije, R., Brimioulle, S., and Dewachter, L. (2014). Biomechanics of the right ventricle in health and disease (2013 grover conference series). *Pulmonary circulation*, 4(3):395–406.

[42] Naeije, R. and Manes, A. (2014). The right ventricle in pulmonary arterial hypertension. *European respiratory review*, 23(134):476–487.

[43] Peacock, A., Murphy, N., McMurray, J., Caballero, L., and Stewart, S. (2007). An epidemiological study of pulmonary arterial hypertension in scotland. *European Respiratory Journal*.

[44] Phatak, N. S., Maas, S. A., Veress, A. I., Pack, N. A., Di Bella, E. V., and Weiss, J. A. (2009). Strain measurement in the left ventricle during systole with deformable image registration. *Medical image analysis*, 13(2):354–361.

[45] Puwanant, S., Park, M., Popović, Z. B., Tang, W. W., Farha, S., George, D., Sharp, J., Puntawangkoon, J., Loyd, J. E., Erzurum, S. C., et al. (2010). Ventricular geometry, strain, and rotational mechanics in pulmonary hypertension. *Circulation*, 121(2):259–266.

[46] Quaife, R. A., Chen, M. Y., Lynch, D., Badesch, D. B., Groves, B. M., Wolfel, E., Robertson, A. D., Bristow, M. R., and Voelkel, N. F. (2006). Importance of right ventricular end-systolic regional wall stress in idiopathic pulmonary arterial hypertension: a new method for estimation of right ventricular wall stress. *European journal of medical research*, 11(5):214.

[47] Rain, S., Andersen, S., Najafi, A., Gammelgaard Schultz, J., da Silva Gonçalves Bós, D., Handoko, M. L., Bogaard, H.-J., Vonk-Noordegraaf, A., Andersen, A., van der Velden, J., et al. (2016). Right ventricular myocardial stiffness in experimental pulmonary arterial hypertension: relative contribution of fibrosis and myofibril stiffness. *Circulation: Heart Failure*, 9(7):e002636.

[48] Rajagopal, S., Forsha, D. E., Risum, N., Hornik, C. P., Poms, A. D., Fortin, T. A., Tapson, V. F., Velazquez, E. J., Kisslo, J., and Samad, Z. (2014). Comprehensive assessment of right ventricular function in patients with pulmonary hypertension with global longitudinal peak systolic strain derived from multiple right ventricular views. *Journal of the American Society of Echocardiography*, 27(6):657–665.

[49] Redington, A. N., Gray, H. H., Hodson, M. E., Rigby, M., and Oldershaw, P. (1988). Characterisation of the normal right ventricular pressure-volume relation by biplane angiography and simultaneous micromanometer pressure measurements. *Heart*, 59(1):23–30.

[50] Reichek, N. (2013). Right ventricular strain in pulmonary hypertension: flavor du jour or enduring prognostic index? *Circulation. Cardiovascular imaging*, 6(5):609.

[51] Shehata, M. L., Harouni, A. A., Skrok, J., Basha, T. A., Boyce, D., Lechtzin, N., Mathai, S. C., Girgis, R., Osman, N. F., Lima, J. A., et al. (2013). Regional and global biventricular function in pulmonary arterial hypertension: a cardiac mr imaging study. *Radiology*, 266(1):114–122.

[52] Smith, B. C., Dobson, G., Dawson, D., Charalampopoulos, A., Grapsa, J., and Nihoyannopoulos, P. (2014). Three-dimensional speckle tracking of the right ventricle: toward optimal quantification of right ventricular dysfunction in pulmonary hypertension. *Journal of the American*

College of Cardiology, 64(1):41–51.

[53] Stenmark, K. R., Meyrick, B., Galie, N., Mooi, W. J., and McMurtry, I. F. (2009). Animal models of pulmonary arterial hypertension: the hope for etiological discovery and pharmacological cure. *American Journal of Physiology-Lung Cellular and Molecular Physiology*, 297(6):L1013–L1032.

[54] Trip, P., Rain, S., Handoko, M. L., Van der Bruggen, C., Bogaard, H. J., Marcus, J. T., Boonstra, A., Westerhof, N., Vonk-Noordegraaf, A., and Frances, S. (2015). Clinical relevance of right ventricular diastolic stiffness in pulmonary hypertension. *European Respiratory Journal*, pages ERJ–01567.

[55] Veress, A. I., Gullberg, G. T., and Weiss, J. A. (2005). Measurement of strain in the left ventricle during diastole with cine-mri and deformable image registration. *Journal of biomechanical engineering*, 127(7):1195–1207.

[56] Vogel-Claussen, J., Skrok, J., Shehata, M. L., Singh, S., Sibley, C. T., Boyce, D. M., Lechtzin, N., Girgis, R. E., Mathai, S. C., Goldstein, T. A., et al. (2011). Right and left ventricular myocardial perfusion reserves correlate with right ventricular function and pulmonary hemodynamics in patients with pulmonary arterial hypertension. *Radiology*, 258(1):119–127.

[57] Wang, Z., Schreier, D. A., Hacker, T. A., and Chesler, N. C. (2013). Progressive right ventricular functional and structural changes in a mouse model of pulmonary arterial hypertension. *Physiological reports*, 1(7).

[58] Xi, C., Latnie, C., Zhao, X., Le Tan, J., Wall, S. T., Genet, M., Zhong, L., and Lee, L. C. (2016). Patient-specific computational analysis of ventricular mechanics in pulmonary arterial hypertension. *Journal of Biomechanical Engineering*, 138(11):111001.

[59] Xi, J., Lamata, P., Shi, W., Niederer, S., Land, S., Rueckert, D., Duckett, S. G., Shetty, A. K., Rinaldi, C. A., Razavi, R., et al. (2011). An automatic data assimilation framework for patient-specific myocardial mechanical parameter estimation. In *International Conference on Functional Imaging and Modeling of the Heart*, pages 392–400. Springer.

[60] Zou, H., Xi, C., Zhao, X., Koh, A. S., Gao, F., Su, Y., Tan, R.-S., Allen, J., Lee, L. C., Genet, M., et al. (2018). Quantification of biventricular strains in heart failure with preserved ejection fraction patient using hyperelastic warping method. *Frontiers in physiology*, 9:1295.

Figure 1: Comparison of peak regional (a) circumferential and (b) longitudinal strains be-

tween control (unstriped) and PAH (striped) groups with (*) denoting that the latter value is statistically lower ($P < 0.05$) than the former. Time traces of RVFW longitudinal strain of the (c) PAH patients and (d) control subjects. Thick line denotes average and error bar denotes standard deviation

Figure 2: Pressure (blue) and volume (red) traces for all simulations. Solid pressure lines give loading conditions for the simulations, while solid red lines show measured volumes of the ventricles. Dots indicate optimized simulated volumes for the time points.

Figure 3: Overall data assimilation errors in the control (circle) and PAH patient (diamond) populations. Comparison between measured and simulated (a) volumes for both the RV (blue) and LV (red); (b) E_{cc} for the LVFW (red), SEPT (green), and RVFW (blue) at all cardiac time points. A $y = x$ line is also plotted to show the zero error reference.

Figure 4: Examples of simulation results from an extensively remodeled pulmonary hypertension patient, RVDEV/LVEDV = 1.75, (left column) and a healthy control (right column). A) PV loop data (open markers) and simulations (solid lines) for the LV (red) and RV (blue). B) Calculated fiber stresses at end diastole, and C) Calculated fiber stresses at end systole.

Figure 5: Analysis of peak RVFW contractility $\gamma_{RVFW,max}$ for control and PAH patient groups. (a) Graphical depiction of $\gamma_{RVFW,max}$ for both controls (diamonds) and patients (black dots) as a function of the ratio of RVEDV/LVEDV. Dashed line shows a linear fit to the PAH patient group ($\gamma_{RVFW,max} = -0.13(\text{RVEDV/LVEDV})+0.44, R^2 = 0.77$). (b) Average $\gamma_{RVFW,max}$ for controls, patients with RVEDV/LVEDV < 1.5 and patients with RVEDV/LVEDV ≥ 1.5. (c) Linear fit of $\gamma_{RVFW,max}$ with RVEDVi ($\gamma_{RVFW,max} = -0.001(\text{RVEDVi})+0.32, R^2 = 0.40$) (d) Linear fit of $\gamma_{RVFW,max}$ with RVEF ($\gamma_{RVFW,max} = 0.39(\text{RVEF})+0.09, R^2 = 0.50$).

Figure 6: Analysis of peak LVFW contractility $\gamma_{LVFW,max}$ for control and PAH patient groups. (a) Graphical depiction of peak LVFW contractility for both controls (diamonds) and patients (black dots) as a function of RVEDV/LVEDV. (b) Average $\gamma_{LVFW,max}$ for controls, patients with RVEDV/LVEDV < 1.5 and patients with RVEDV/LVEDV ≥ 1.5.

Figure 7: Comparison of passive tissue stiffness parameter a between control and the PAH groups in the (a) LVFW + SEPT and (b) RVFW regions.

Figure 8: Comparison of peak myofiber wall stress $\sigma_{ff_{max}}$ between control and the PAH groups in the (a) LVFW and (b) RVFW regions.